THE GEOLOGICAL SOCIETY OF AMERICA®

Clay mineralogical constraints on weathering in response to early Eocene hyperthermal events in the Bighorn Basin, Wyoming (Western Interior, USA)

Chaowen Wang[1,2,†], Rieko Adriaens[3], Hanlie Hong[4], Jan Elsen[3], Noël Vandenberghe[3], Lucas J. Lourens[2], Philip D. Gingerich[5], and Hemmo A. Abels[6,†]

[1]*Gemmological Institute, China University of Geosciences, Wuhan, 430074, P.R. China*
[2]*Department of Earth Sciences, Utrecht University, Heidelberglaan 2, 3584 CS, Utrecht, Netherlands*
[3]*Department Earth and Environmental Sciences, KU Leuven, Celestijnenlaan 200E, B-3001 Leuven, Belgium*
[4]*State Key Laboratory of Biogeology and Environmental Geology, China University of Geosciences, Wuhan, 430074, P.R. China*
[5]*Department Earth and Environmental Sciences, University of Michigan, Ann Arbor, Michigan 48109, USA*
[6]*Department Geosciences and Engineering, Delft University of Technology, Stevinweg 1, 2628 CN, Delft, Netherlands*

ABSTRACT

Series of transient greenhouse warming intervals in the early Eocene provide an opportunity to study the response of rock weathering and erosion to changes in temperature and precipitation. During greenhouse warming, chemical weathering is thought to increase the uptake of carbon from the atmosphere, while physical weathering and erosion control sediment supply. A large ancient greenhouse warming event is the Paleocene-Eocene Thermal Maximum at 56 Ma. In many coastal sites, an increase in the abundance of kaolinite clay during the Paleocene-Eocene Thermal Maximum is interpreted as the result of reworking from terrestrial strata due to enhanced runoff caused by increased seasonal precipitation and storminess during a time of decreased vegetation cover. In the continental interior of North America, Paleocene-Eocene Thermal Maximum paleosols show more intense pedogenesis and drying, which are indicated by deeply weathered and strongly oxidized soil profiles. The weathering and oxidation could be related to temperature and precipitation changes, but also to increased time available for weathering and increased soil permeability in coarser sediment.

Here, we provide evidence for enhanced climate seasonality, increased erosion of proximal laterites and intrabasinal floodplain soils, and a potential slight increase in chemical weathering during the smaller early Eocene hyperthermals (Eocene Thermal Maximum 2, including H1 and H2) postdating the Paleocene-Eocene Thermal Maximum, for which no previous clay mineral data were available. Hyperthermal soil formation at the site of floodplain deposition causes a similar, insignificant clay mineralogical change as occurred during the background climates of the early Eocene by showing small increases in smectite and decreases in illite-smectite and illite. Remarkably, the detrital sediments during the hyperthermals show a similar pedogenic-like increase of smectite and decreases of mixed-layer illite-smectite and illite, while the kaolinite and chlorite proportions remained low and unchanged. Since sedimentation rates and provenance were similar during the events, enhanced smectite neoformation during soil formation in more proximal settings, and associated reworking, is the likely process causing this clay mineralogical change. The hundreds to thousands of year time scales at which individual paleosols were formed were probably too short for significant alteration of the rocks by in situ chemical weathering despite changing climates during the two post–Paleocene-Eocene Thermal Maximum greenhouse warming episodes. The relatively small signal, however, raises the question of whether increased chemical weathering can indeed be a strong negative feedback mechanism to enhanced greenhouse gas warming over the time scales at which these processes act.

INTRODUCTION

The latest Paleocene and earliest Eocene were characterized by multiple transient episodes of greenhouse warming, called hyperthermals, which were triggered by rapid addition of exogenic carbon into the ocean-atmosphere carbon pool (Dickens et al., 1995; Kurtz et al., 2003; Svensen et al., 2004). The largest of these hyperthermals at ca. 56 Ma is known as the Paleocene-Eocene Thermal Maximum. The Paleocene-Eocene Thermal Maximum reflects a major perturbation of Earth's oceans and atmosphere associated with a warming of the deep sea by ~4–5 °C and warming of the global surface oceans at all latitudes by ~5–9 °C (McInerney and Wing, 2011). This event lasted ~150–200 k.y., including full recovery, and coincided with the release of significantly more than 2000 Gt of isotopically light carbon, resulting in a negative carbon isotope excursion in organic and carbonate substrates hosted in both marine and terrestrial strata (e.g., Zachos et al., 2005). The consequences of the exogenic carbon during the Paleocene-Eocene Thermal Maximum resulted in dramatic ocean acidification, climate warming, mass extinction of deep-sea benthic foraminifers, and overturn, diversification, and dwarfism of mammalian faunas (Maas et al., 1995; Wing et al., 1995; Bains et al., 1999;

†Corresponding authors: cwwang_cug@aliyun.com, h.a.abels@tudelft.nl.

GSA Bulletin; July/August 2017; v. 129; no. 7/8; p. 997–1011; doi: 10.1130/B31515.1; 8 figures; Data Repository item 2017140; published online 28 April 2017.

McInerney and Wing, 2011; Zachos et al., 2005). However, the Paleocene-Eocene Thermal Maximum and the subsequent, smaller hyperthermal events, including the Eocene Thermal Maximum 2 and H2, had different magnitudes of carbon isotopic excursion (Lourens et al., 2005; Sluijs et al., 2009; Stap et al., 2009; Abels et al., 2012, 2016) but had a coherent relationship, suggesting that the carbon isotope change in the exogenic carbon pool was similarly related to deep-sea warming during these events (Stap et al., 2010; Lauretano et al., 2015; Abels et al., 2016). Hence, it remains uncertain whether the climatic and environmental response during the Eocene Thermal Maximum 2 and H2 was similar to that of the well-studied Paleocene-Eocene Thermal Maximum.

Enhanced continental weathering and erosion during the hyperthermals have been thought to be important consequences, since the warming leads to an enhanced continental hydrological cycle. Apart from carbonate dissolution and subsequent limestone deposition, continental weathering is seen as the main mechanism of carbon removal from the atmosphere (Kump et al., 2000; Nicolo et al., 2007; Bowen and Zachos, 2010). The degree and pathways of weathering can be determined from clay and bulk mineralogy of terrestrial and marine sediments. For instance, kaolinite is considered to be a typical weathering product formed under perennial warm and wet conditions. Widespread kaolinite increases near the Paleocene-Eocene boundary in many marginal marine sections have been interpreted as intensified chemical weathering, such as from the Tethys (Bolle and Adatte, 2001; Ernst et al., 2006), the Arctic Ocean (Dypvik et al., 2011), the northern Atlantic Ocean (Gibson et al., 2000; John et al., 2012), and Antarctica (Robert and Kennett, 1994). These findings could be alternatively attributed to strongly increased seasonal precipitation and increases in detrital kaolinite rather than being authigenic in character (McInerney and Wing, 2011; John et al., 2012), because kaolinite increases were coeval with strongly enhanced terrestrial sediment input, likely from increases in river discharge and nutrient supply, and freshening of surface waters during the Paleocene-Eocene Thermal Maximum (Sluijs et al., 2008, 2009; Zacke et al., 2009; Soliman et al., 2011). High-resolution clay mineralogical records across the Paleocene-Eocene Thermal Maximum boundary show sharp increases in the kaolinite/smectite ratio and $\delta^{18}O_{Clays}$ values coeval with a negative shift in $\delta^{13}C$ (John et al., 2012). These changes occur less than 2 k.y. from the start of the Paleocene-Eocene Thermal Maximum, seemingly too quick for kaolinization by pedogenic processes, indicating a detrital and/or mixed origin of clay mineral changes during the Paleocene-Eocene Thermal Maximum (John et al., 2012). It supports a dominance of physical weathering and erosion over chemical weathering in the Paleocene-Eocene Thermal Maximum interval along the east coast of North America.

The well-studied Paleocene-Eocene Thermal Maximum archives from continental interiors are mostly North American. There, drier and likely more seasonal climates seem to have dominated the Paleocene-Eocene Thermal Maximum (Wing et al., 2005; Foreman et al., 2012; Kraus et al., 2013). Paleosol characters and bulk oxide contents in the Bighorn Basin (Wyoming) during the Paleocene-Eocene Thermal Maximum indicate decreased soil moisture, in line with lower mean annual precipitation estimates using leaf area analysis (Wing et al., 2005; Kraus and Riggins, 2007; Kraus et al., 2013) and ichnofossil assemblages (Smith et al., 2008). The sedimentology of channel-belt sandstones from the Paleocene-Eocene Thermal Maximum interval in the Bighorn Basin is consistent with stronger precipitation oscillations leading to decreased overbank cohesiveness and strong runoff pulses redistributing sediment within the basin (Foreman, 2014). In western Colorado, strong progradation of coarse-grained clastics indicates rapid increases in sediment flux and discharge, interpreted to be triggered by shifts in vegetation regime and enhanced monsoonal precipitation (Foreman et al., 2012). In central Utah, more arid climates are interpreted from oxygen isotope profiles in soil carbonate and water (Bowen and Bowen, 2008; Van De Velde et al., 2013). Intense pedogenesis and increases in kaolinite contents in a record ascribed to the Paleocene-Eocene Thermal Maximum in the Williston Basin (North Dakota) are thought to point to intensified terrestrial weathering and more humid conditions (Clechenko et al., 2007). Knowledge of regional climate and continental rock weathering changes during the Paleocene-Eocene Thermal Maximum thus remains sparse, while the impact of the smaller hyperthermals that postdate the Paleocene-Eocene Thermal Maximum, such as Eocene Thermal Maximum 2 and H2, remains to be resolved.

Here, we report on changes in rock weathering as recorded by bulk and clay mineralogy and sediment petrography of the floodplain sediments deposited across the Eocene Thermal Maximum 2 and H2 hyperthermal events in the subtropical Bighorn Basin, northeastern Wyoming, United States. We first constructed a method with which to evaluate the clay mineral changes related to in situ soil formation in the aggrading fluvial floodplain records. Next, we applied this method to evaluate the climate impact of the smaller hyperthermals, Eocene Thermal Maximum 2 and H2, which postdated the Paleocene-Eocene Thermal Maximum, on detrital mineralogy and in situ chemical weathering in the soil profiles. With these, we evaluated whether enhanced weathering might act as a negative feedback during greenhouse warming episodes.

GEOLOGICAL SETTING AND SECTION

The Bighorn Basin is located in northwestern Wyoming, United States, and it is bounded by the Beartooth and Absaroka Mountains to the west, Owl Creek Mountains to the south, and Bighorn Mountains to the east (Fig. 1). Major uplift of the surrounding mountains during the Paleogene occurred in two episodes—one during the mid-late Paleocene, and one during the mid-early Eocene (Thomas, 1965; Fanshawe, 1971). Both of these uplift events were outside the time period of interest for this study.

The fluvial Willwood Formation is of early Eocene age, while its base can be latest Paleocene. Paleocurrent directions were from the west and south of the basin (Fig. 1; Neasham and Vondra, 1972). These mountain ranges include Precambrian granites and granite-gneiss basement rocks and a wide variety of sedimentary rocks, such as Cambrian sandstones, Ordovician dolomites, Devonian carbonates (dolomites and limestones) and shales, Pennsylvanian sandstones, shales, and dolomites, Permian sandstones and carbonates, Triassic red siltstones, shales, and evaporites, Jurassic evaporites and red shales, and Cretaceous sandstones and shales (Thomas, 1965). The Willwood Formation along the western mountains consists of marginal alluvial-fan conglomerates. These conglomerates consist of igneous, metamorphic, and sedimentary rock fragments at the piedmont of the Beartooth Mountains, while they are composed of quartzite pebbles and cobbles along the Absaroka Mountains (Neasham and Vondra, 1972).

Toward the center of the Bighorn Basin, the Willwood and preceding Paleocene Fort Union Formations are mainly comprised of channel-belt sheet sandstones and floodplain sandstones, siltstones, and clayey mudstones. Strong grain-size trends occur from the south to north in the center of the Bighorn Basin. The southern areas, such as Sand Creek Divide and Elk Creek, are much more clay-rich than the northern McCullough Peaks and Polecat Bench areas (Kraus, 2002; Kraus and Riggins, 2007). Mean sedimentation rates in the basin center are estimated at 330 m/m.y. (Abels et al., 2013).

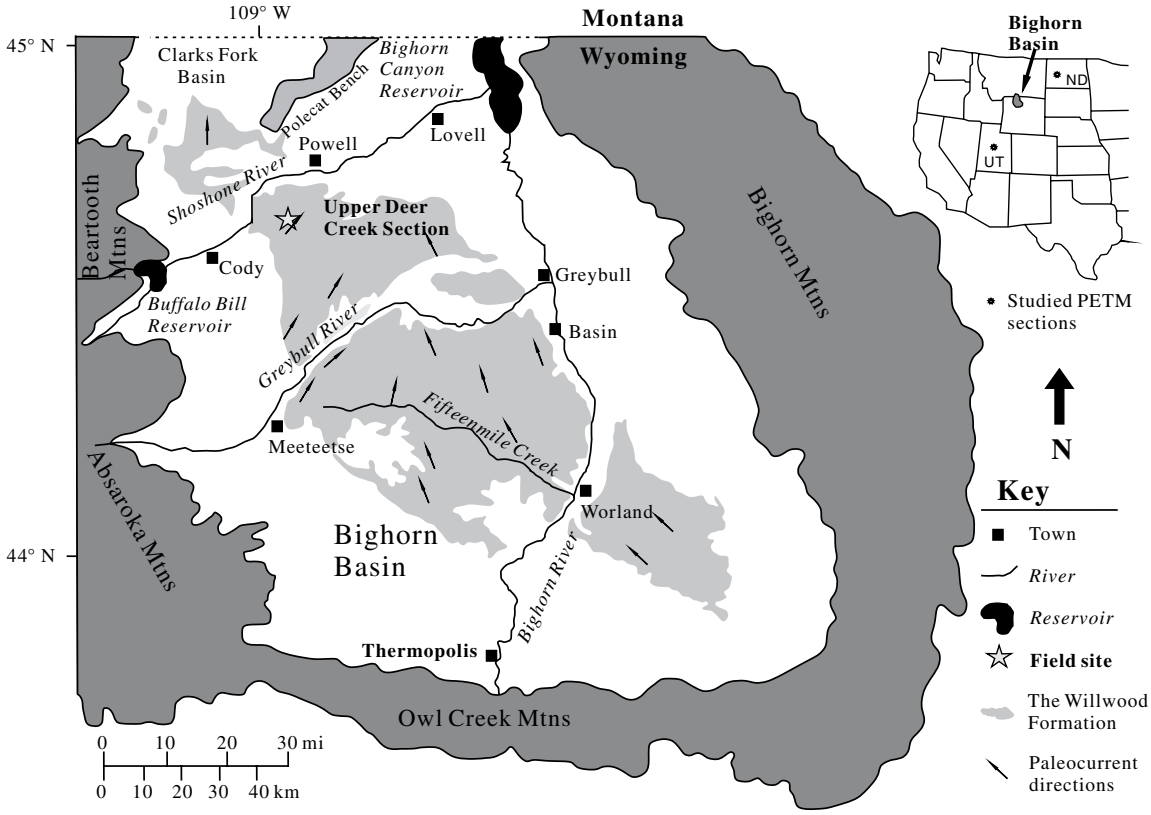

Figure 1. Map of Bighorn Basin showing the distribution of the basin and surrounding mountains as well as the location of Upper Deer Creek section (redrawn after Smith et al., 2008; Neasham and Vondra, 1972). The Willwood Formation in the center of the Bighorn Basin is shown in light gray with paleocurrent direction marked. The studied Upper Deer Creek section is located north of Bighorn Basin. Inset: The localities of studied Paleocene-Eocene Thermal Maximum (PETM) sections in Utah (UT) and North Dakota (ND) are indicated.

The floodplain sediments of the Willwood Formation consist of alternations of heterolithic sandy deposits showing weak or no pedogenic impact and mudrock deposits showing signs of strong in situ pedogenesis (Kraus and Aslan, 1993; Kraus and Gwinn, 1997). The heterolithic deposits have been interpreted as avulsion belt deposits overlying the mudrocks, which in turn have been interpreted as overbank deposits with relatively low sedimentation rates allowing moderate to strong paleosol development (Bown and Kraus, 1987; Kraus and Aslan, 1993; Kraus and Gwinn, 1997; Abels et al., 2013). The lateral consistency of overbank and avulsion belt deposits, the vertical persistence of the thickness of the overbank-avulsion sedimentary sequences, and the occurrence of the overbank-avulsion sequences at 20 k.y. time scales have been used to link overbank-avulsion sequences to climate change related to precession cyclicity (Abels et al., 2013).

This study focuses on the 135-m-thick Upper Deer Creek (UDC) section in the McCullough Peaks area of the northern Bighorn Basin, Wyoming. The section is located at 44°36′34.7″N, 108°49′74.1″W. In this section, heterolithic and mudrock deposits consisting mainly of sandy siltstones and claystones are reciprocally interbedded, while large channel-belt sandstone bodies were avoided (for detail, see Abels et al., 2013; Fig. 2). Distinct purple beds in the section characterize the Eocene Thermal Maximum 2–H2 interval. The carbon isotope excursions that have been related to the Eocene Thermal Maximum 2 and H2 are reported within biostratigraphic, magnetostratigraphic, and cyclostratigraphic frameworks (Abels et al., 2012).

SAMPLING AND METHOD

Samples and lithological descriptions are from the study of Abels et al. (2012). Field descriptions include grain size, matrix color, size

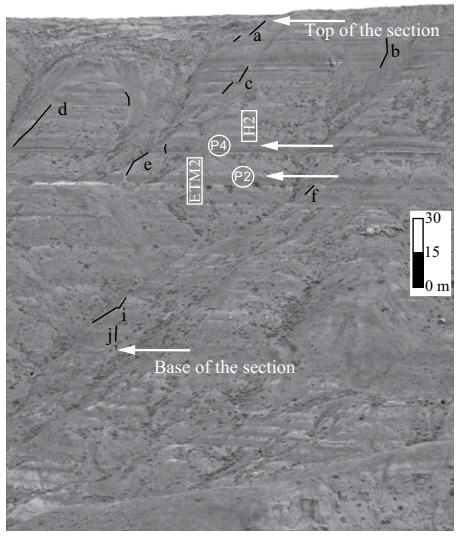

Figure 2. Field image of Upper Deer Creek section showing cyclic lithology and color changes. The bases of Eocene Thermal Maximum 2 (ETM2) and H2, and the purple layers labeled 2 and 4 marking the hyperthermal events are indicated in white. The subsections are numbered a to f and i, while subsections g and h are invisible because of the angle from which the photograph was taken.

and color of mottling, presence, abundance, and size of carbonate nodules, and abundance and size of slickensides, as well as recognition of paleosol profiles. The color determination of matrix and mottles was based on the Revised Standard Soil Color Charts of Oyama and Takehara (1970). In total, 148 clay and bulk mineralogy samples were collected every 50–100 cm (average 77 cm) throughout the 135-m-thick section. Samples were spaced 1.5–3 k.y. based on the virtual case sedimentation rates, which were constant between those of overbank and avulsion deposits.

Grain-Size Analysis

Thirty-five samples including sandstone/siltstone, mudstone, and paleosols were subject to grain-size analysis. Carbonate and organic matter were removed prior to the analysis. Samples were treated with 10 mL 30% H_2O_2 to remove all organic material and 10 mL 10% HCl to remove calcium carbonate. $Na_4P_2O_7{\cdot}10H_2O$ was used to further disperse grains. Before the actual measurements were done, all samples were treated with an ultrasonic transducer for 5 min. Grain-size analysis was carried out in the sedimentological laboratory, Vrije Universiteit (VU), Amsterdam. Grain-size statistics were gathered using a Sympatec HELOS/KR laser-diffraction particle size measurer with advanced wet disperser QUIXEL. This resulted in grain-size distributions ranging from 0.1 to 2000 µm, divided into 57 sections.

Scanning Electron Microscope

Scanning electron microscopy (SEM) was employed on sandy mudstones, clayey mudstones, and paleosol samples from two soil horizons with ~1 g for each block using a JEO JCM-6000 NeoScope Benchtop SEM at 10 or 15 kV accelerating voltage at Utrecht University, Netherlands. An energy dispersive spectrometer (EDS) was used to determine the elementary composition of the minerals with an accelerating voltage of 15 kV and a beam current of 1 nA.

Preparation for Bulk and Clay Mineralogical Analysis

Approximately 50 g aliquots of each sample were ground and homogenized to <10–15 µm using an automated tungsten-carbide disc mill (Herzog HSM-HTP) at Utrecht University, Netherlands. The bulk sample preparation (after Środoń et al., 2001) was conducted at Leuven University, Belgium. Then, 2.7 g of well-homogenized samples were mixed with 0.3 g of ZnO and ground in a McCrone Mill for 5 min. The residue was washed with 100% absolute ethyl alcohol to accelerate drying, after which the dry sample was side loaded into an aluminum sample holder to ensure random orientation of crystallites (Środoń et al., 2001). Isolation of clay species <2 µm and <0.2 µm was in accordance with the procedure proposed by Jackson (1975). During the procedure, carbonates, organic matter, and iron oxides were removed, after which <2 µm and <0.2 µm fractions were isolated using sequential centrifugation and ultrasonic treatments. These different fractions were obtained to analyze the clay mineral distributions in different grain-size fractions. Ca-saturated clay species were achieved by washing the samples three times with 1 mol/L $CaCl_2$, which was subsequently removed via dialysis using a semipermeable membrane. The Ca-saturation procedure was to convert Na-saturated samples, which were produced when Na-bearing reagents were used as carbonate-dissolving and clay-flocculating agents, to the Ca form to prevent peak overlaps between vermiculite and Na-smectite and between mixed-layer illite-smectite and mixed-layer illite-vermiculite in the X-ray diffraction (XRD) patterns. Oriented clay slides of <2 µm and <0.2 µm fractions were prepared by sedimenting clay slurries onto glass slides. Eight representative samples throughout the section from low to high were also selected for the "vermiculite test." Clay minerals have different capacities for cation exchange because of their charge differences. Mg- and K-saturated treatments combined with heating or saturation of glycerol (G), called the vermiculite test, are used to identify smectite, vermiculite, and chlorite, which have similar 001 reflections. To distinguish chlorite from vermiculite, K-saturation combined with heating to 300 °C for 1 h was applied. Such a procedure will collapse all expandable layers (smectite and vermiculite) to 10 Å, while chlorite will stay at ~14 Å in the XRD pattern. Meanwhile, Mg-saturation in combination with saturation of glycerol was utilized to subsequently distinguish smectite from vermiculite, since vermiculite will remain at ~14 Å, while smectite will swell to 17.7 Å or more.

Identification and Quantification of Bulk and Clay Minerals

Bulk and clay mineral samples were identified by XRD at KU Leuven, Belgium, using a PW 1830 diffractometer with Cu-Ka radiation in a Bragg-Brentano theta-2theta setup equipped with a graphite crystal monochromator and proportional detector type PW3011/00. Bulk powders and clay slides were scanned under 45 kV and 30 mA working conditions with a step size of 0.02° 2θ/s and speed of 2 s/step, ranging from 5 to 65° 2θ and from 2 to 47° 2θ, respectively. Clay slides were examined following air-drying (AD) and ethylene-glycol (EG) saturation.

Identification of bulk mineralogy was carried out following characteristic reflections for each mineral. Quantification of bulk mineral proportions was done using the QUANTA© (Chevron ETC) software with an estimated error of 1% for nonclays and within 3% for clays, respectively.

Clay mineral compositions were mainly identified based on the 001 reflections on combined AD and EG XRD diagrams (Fig. 3). The peak at 14.5–15.5 Å in AD slides, which then shifts to 16.8–17 Å after EG treatment, was recognized as an expandable mineral such as smectite or vermiculite. Illite remained at ~10 Å in both AD and EG treated slides. Irregular mixed-layer illite-smectite was identified here based on the broad peaks between the 002 and 003 reflections of smectite and illite. Because chlorite occurs in small amounts, the 003 reflection of chlorite (4.74–4.76 Å) was utilized to avoid overlaps of the 001 and 002/004 reflections with smectite and kaolinite, respectively. The 001 reflection at 7.13 Å was identified as kaolinite. After Mg-saturation in combination with saturation of glycerol (24 h, 110 °C), the 001 reflection of smectite at 14.5 Å shifted to 18.4 Å, which identified the expandable mineral as smectite. This was supported by K-saturation and heating to 300 °C for 1 h. After this treatment, the stable chlorite reflection moved to ~14 Å. Hence, no indications were found for the presence of vermiculite.

Quantification of clay mineral proportions was performed using the program SYBILLA© (Chevron), with the difference between the fitting results of AD and EG states within 3%. The calculated XRD profile was composed of all the simulated clay species that were identified (Fig. 4). A fit was accepted when a close match was achieved for peak position, ratios, and shapes both in glycolated and air-dried states by adjusting realistic parameters for each layer type, proportions of each clay species, and proportions of the different layer types in mixed-layer illite-smectite, and when both fits produced the same or similar quantitative compositions using the same layer-type parameters and proportions (Sakharov et al., 1999). Through all the samples, two kinds of "kaolinite" were used here to fit the experimental data well. As shown in Figure 4, one "kaolinite" has larger mean crystallite thickness showing a narrow peak at 7.14 Å, and the other one has a smaller mean crystallite thickness and shows a broad peak at 7.16 Å. The proportion of kaolinite was the sum of both kaolinites. Modeling smectite is often not sufficient to be able to match the experimental pattern with only

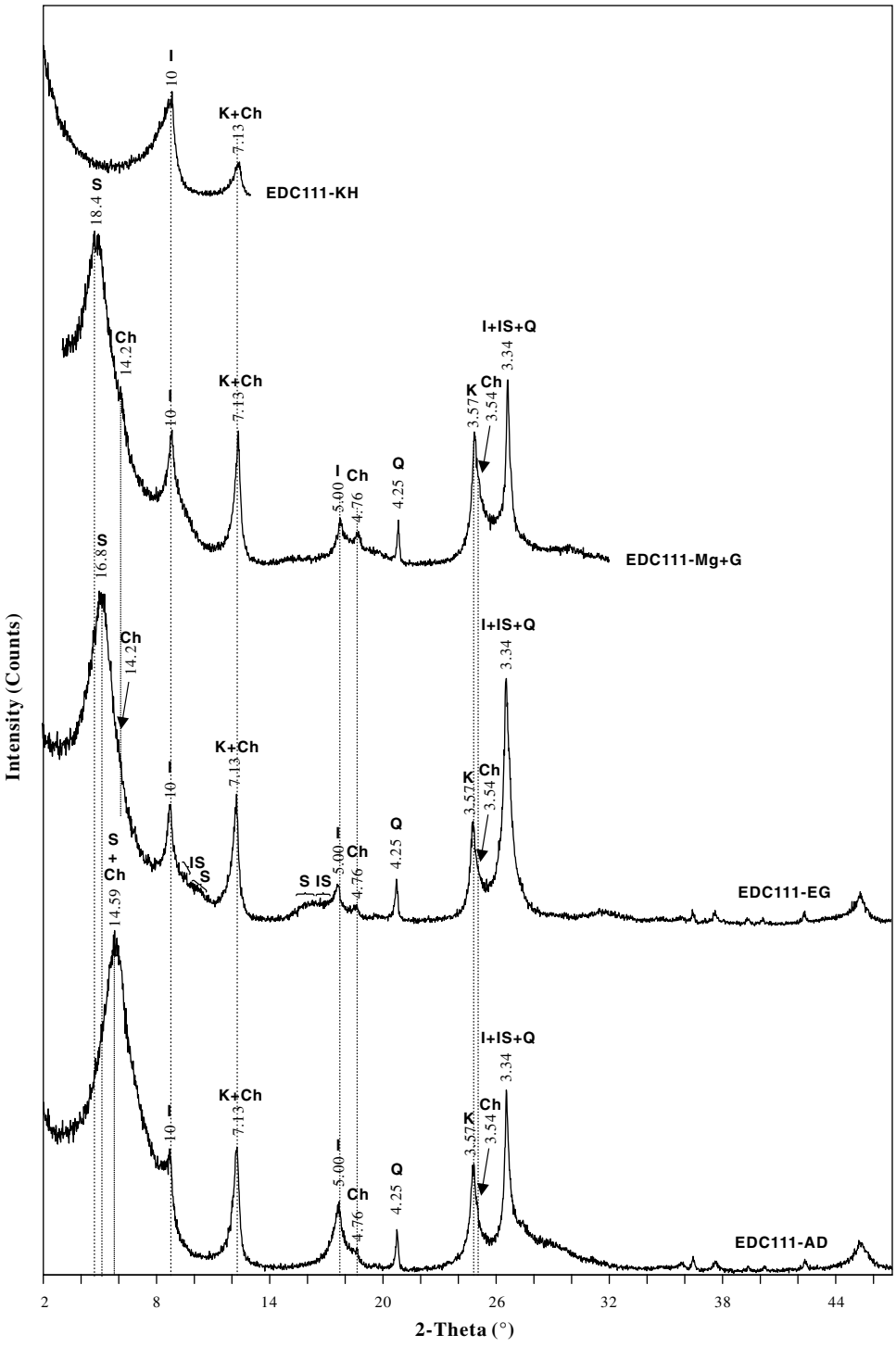

Figure 3. Example of multitreatment X-ray diffraction (XRD) patterns of sample UDC111 (27.75 m, clayey mudstone) from the Upper Deer Creek (UDC) section. S—smectite, Ch—chlorite, IS—mixed-layer illite-smectite, I—illite, K—kaolinite, Q—quartz, AD—air-dried, EG—ethylene-glycol saturated, Mg+G—magnesium and glycerol saturated, KH—potassium saturated and 300 °C heating. Note that the peak shifts from 14.6 Å to 16.8 Å and further shifts to 18.4 Å after EG and Mg+G treatments, respectively. This peak, however, collapses to 10 Å after KH treatment, indicating smectite is present in the sample rather than chlorite and vermiculite. The peak at ~14 Å stays without a shift to 10 Å after KH treatment, indicating the presence of chlorite. Irregular mixed-layer illite-smectite is identified here based on the broad peaks between the 002 and 003 reflections of smectite and illite. Illite stays at ~10 Å and kaolinite stays at ~7.1 Å throughout all the treatments above.

one layer type. Because of a larger expression of charge heterogeneity and relative humidity in the air-dried state, swelling clays such as smectite and mixed-layer illite-smectite have different proportions of one and two layers of the saturating fluid (water and ethylene glycol). Smectite was modeled using both 2-EG and 1-EG interlayers in EG patterns with a typical ratio ranging from 85:15 to 97:3. Similar ratios of 2-water and 1-water were used when modeling the AD patterns. Similar to smectite, irregular mixed-layer illite-smectite, which typically has a ratio of illite to smectite between 66:34 and 80:20, also was modeled using both two and one interlayers of EG molecules and water for the part of smectite when fitting the profile, with 6%–52% of one interlayer EG molecules and water in EG and AD patterns, respectively.

Soil Development Index

The soil development index (SDI) was quantified after the method of Abels et al. (2013). The field lithology information, horizontal development, profile development and thickness, and morphological features, including color, soil nodule development, mottling, and nature of contacts within the profile, make up the basic

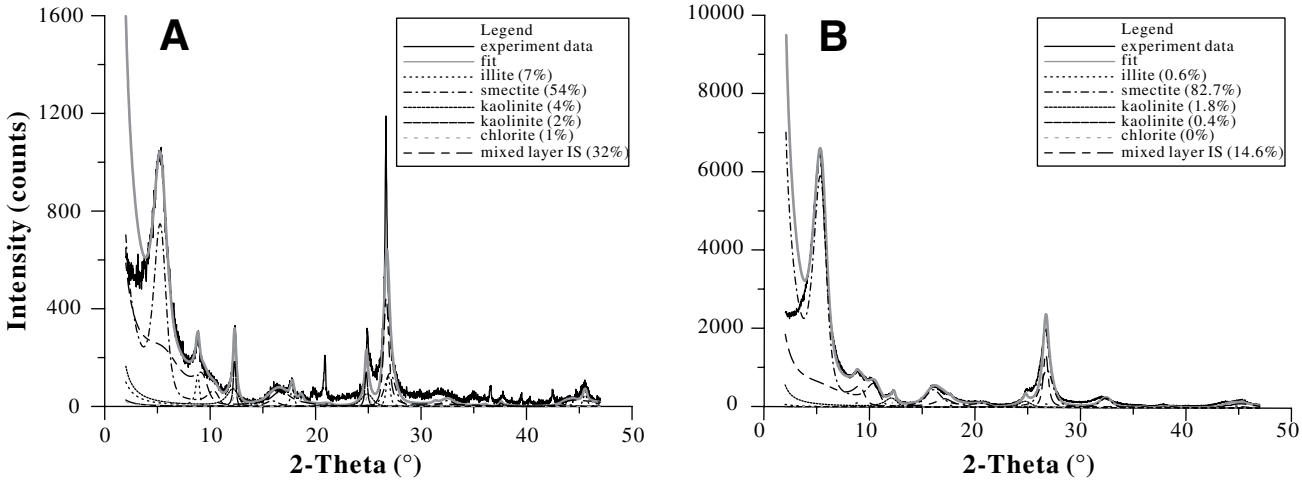

Figure 4. Examples of comparison between experimental and calculated X-ray diffraction (XRD) profiles using program SYBILLA (©Chevron). (A) Example of fitting profile for sample UDC-208 (52 m depth, sandy mudstone) of <2 µm fraction based on ethylene-glycol–saturated (EG) state. (B) Example of fitting profile for sample UDC-208 of <0.2 µm fraction based on the EG state. Both kaolinites with larger and smaller mean crystallite thickness were used here to fit profiles well. Note that uncertainties (clay minerals on average) of <2 and <0.2 µm fractions are 1.2% and 0.8%, respectively. IS—illite-smectite.

quantification of soil development. Four categories of SDI were classified here based on the level of pedogenesis. Simply, intervals without pedogenic modification were assigned an SDI of 0. Rock with incipient pedogenesis, medium-developed pedogenesis, well-developed pedogenesis, and very well-developed pedogenesis was assigned SDI of <0.5, 1–2, 2–3, and 3–4, respectively.

Statistical Methodology for Clay Mineralogical Data

The river floodplain sediments studied here show strong lithological changes through time tied to overbank and avulsion sedimentation and hyperthermal events (Kraus and Riggins, 2007; Abels et al., 2012, 2013, 2016). In order to better understand factors that may have an impact on the clay mineral proportions, we first analyzed the clay mineralogical distributions over different grain-size classes by selecting the samples that showed no or very limited soil development. Subsequently, the impact of soil development was tested for these samples, all from outside the hyperthermal events. Last, the impact of the hyperthermals was tested by evaluating clay mineralogy distributions of the samples showing no or very limited and medium and intense soil development, respectively. The results of clay mineral distributions were then compared between those within and those outside the hyperthermal events.

An analysis of variance (ANOVA) was carried out in MS Excel 2010 to evaluate the proportional similarities/differences of clay minerals, with statistical significance defined as $p < 0.05$. The similarities/differences were accepted at a 95% confidence level if the p value was less than 0.05.

RESULTS

Grain Size, Bulk Mineralogy, and Sediment Microtextures

Grain-Size Distributions

We divided field-based grain-size descriptions into four grain-size classes, fine sand to sandy silt, (clayey) silt, silty clay, and clay. The fine sand to sandy-silt class is mostly related to avulsion and crevasse-splay deposits, and the remaining three classes are mostly related to true overbank deposition. Grain-size measurements using laser-diffraction technology showed that the fine-sand-to-sandy-silt bin on average consists of 32% clay or finest silt (<8 µm), 37% silt, and 31% sand (Table DR1 in the Data Repository 1[1]). The clayey-silt bin consists of 33% clay or finest silt, 59% silt, and 8% sand. The silty-clay and clay are composed of 63% and 82% clay and finest silt, 33% and 17% silt, respectively, and negligible sand proportions. The classes related to the avulsion and crevasse-splay deposits are hereafter labeled as sandy mudstones, and the classes related to overbank deposits are hereafter labeled as clayey mudstones. The clayey-mudstones group is divided into mudstones showing no or limited signs for (severe) pedogenesis and mudstones that show pedogenesis based on field observations and SDI.

Bulk Mineral Composition

The bulk mineral composition of the floodplain sediments in the Upper Deer Creek section is dominated on average by 53.8% clay minerals (13.4%–76%), 36.3% quartz (16%–76%), and 3.6% K-feldspar (0.5%–9%; Fig. 5; Table DR2 [see footnote 1]). Quartz, K-feldspar, plagioclase, calcite, and dolomite dominate the sandy mudstones. Plagioclase (0%–6%), calcite (0%–10%), and dolomite (0%–6%) are less common and show higher values in the sandy mudstones with respect to the clayey mudstones. Goethite (0%–4%), anatase (0%–0.9%), and pyrite (0%–0.9%) occur in (very) minor proportions. Barite is present in two samples with proportions of 2% and 3%, respectively. The abundance of quartz and clay minerals exhibits a strong inverse relationship in all samples (Figure DR1 [see footnote 1]).

Sediment Microtexture

The clayey mudstones and sandy mudstones show a similar microtexture while exhibiting differences in grain size and mineral morphology. The sediments are mainly composed of detrital

[1]GSA Data Repository item 2017140, additional detail on data tables DR1–DR3 with the grain-size, bulk and clay mineralogy, Figures DR1–DR3, and Tables DR1–DR3, is available at http://www.geosociety.org/datarepository/2017 or by request to editing@geosociety.org.

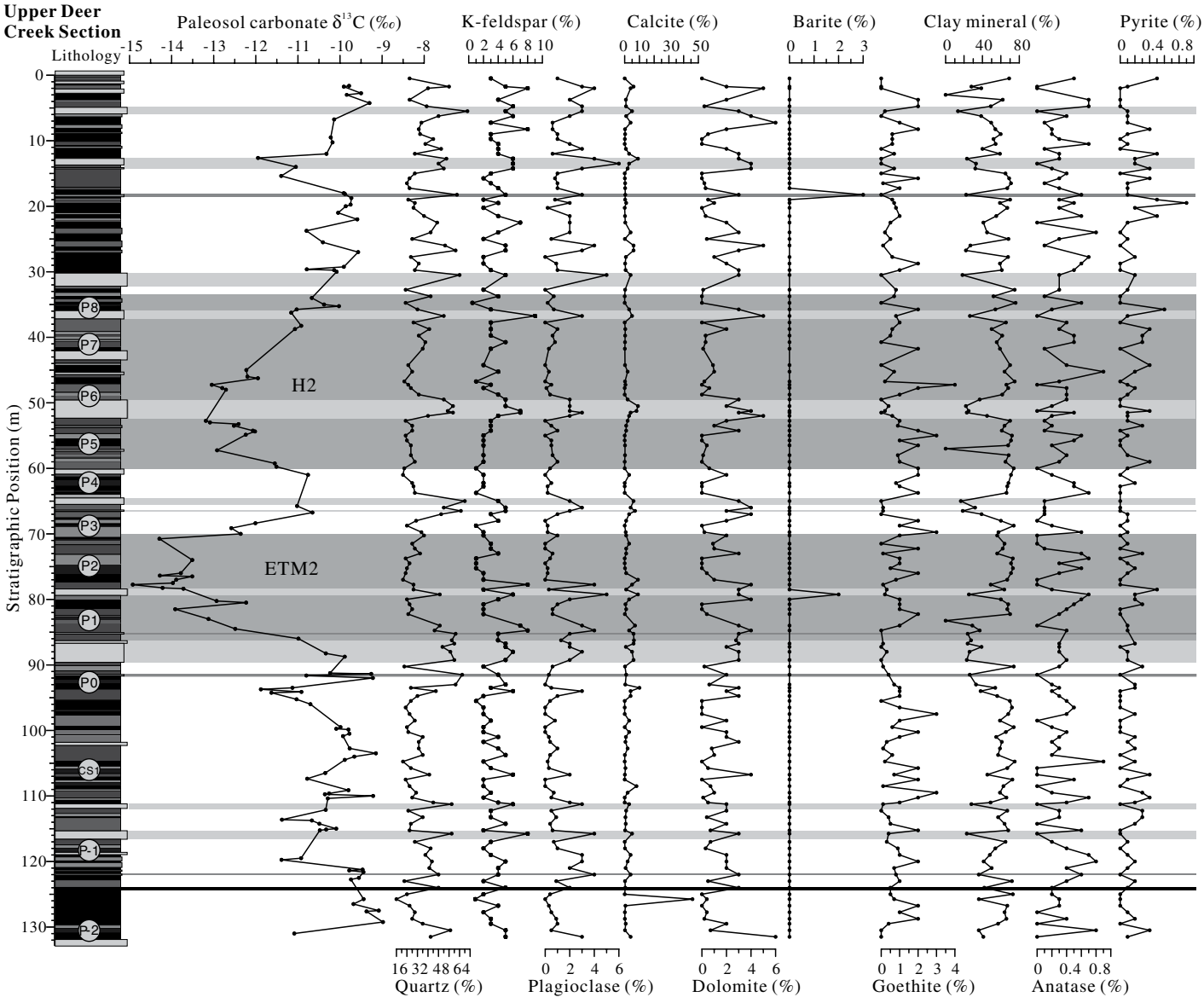

Figure 5. Mineral proportions of bulk sediments along the Upper Deer Creek (UDC) section. Note that lithological log consists of cyclic sand/silt, mudstone, and paleosols. A distinct cycle, at a scale of ~7 m, is paced by the orbital climate forcing due to the ~21 k.y. precession cycle (Abels et al., 2012, 2013, 2016). Records of paleosol carbonate $\delta^{13}C$ are indicated in the first column (Abels et al., 2012). A remarkable change of bulk minerals is related to the change of lithology with quartz, K-feldspar, plagioclase, calcite, and dolomite enriched in sands/silts marked in tan bars and clay minerals in mudstones. Observed hyperthermals, Eocene Thermal Maximum 2 (ETM2) and H2, are indicated in gray and show no significant change in bulk minerals.

particles that are matrix-supported by clay. The particles show subangular to less common well-rounded and spherical shapes (Fig. 6A). Clay minerals occur as thin platy shapes, exhibit random directions of the 001 plane, and show different character in different grain-size classes (Fig. 6B). In the sandy mudstones, clay particles such as mica and kaolinite can be as large as 30–50 µm in diameter (Figs. 6C and 6D). Mica shows subangular shapes. Kaolinite displays booklet-shaped and crooked debris with poorly developed pseudohexagonal appearance and limited extension in the *c* orientation. Smectite and/or mixed-layer illite-smectite show irregular surfaces where smectite has been transformed to curled thin flakes with embayed edges (Fig. 6E). Single crystals of calcite exhibit subrounded morphology, well-developed rhombohedra, and intensively dissolved surfaces forming rhombic pits (Fig. 6F).

Clay minerals in the clayey mudstones show intensively dissolved surfaces. The dissolved clay particles exhibit embayed edges and streamlined outlines (Fig. 6G). These minerals are likely illite and mixed-layer illite-smectite, as also suggested by EDS showing particles rich in K with minor Na and others rich in Mg and Fe, and minor K, besides Si, Al, and O (Figure DR2 [see footnote 1]).

Rarely, clay minerals in soil B horizons show distinct morphologies as incipient honeycomb and flake shapes of smectite in clayey mudstones (Fig. 6H). Generally, these smectite

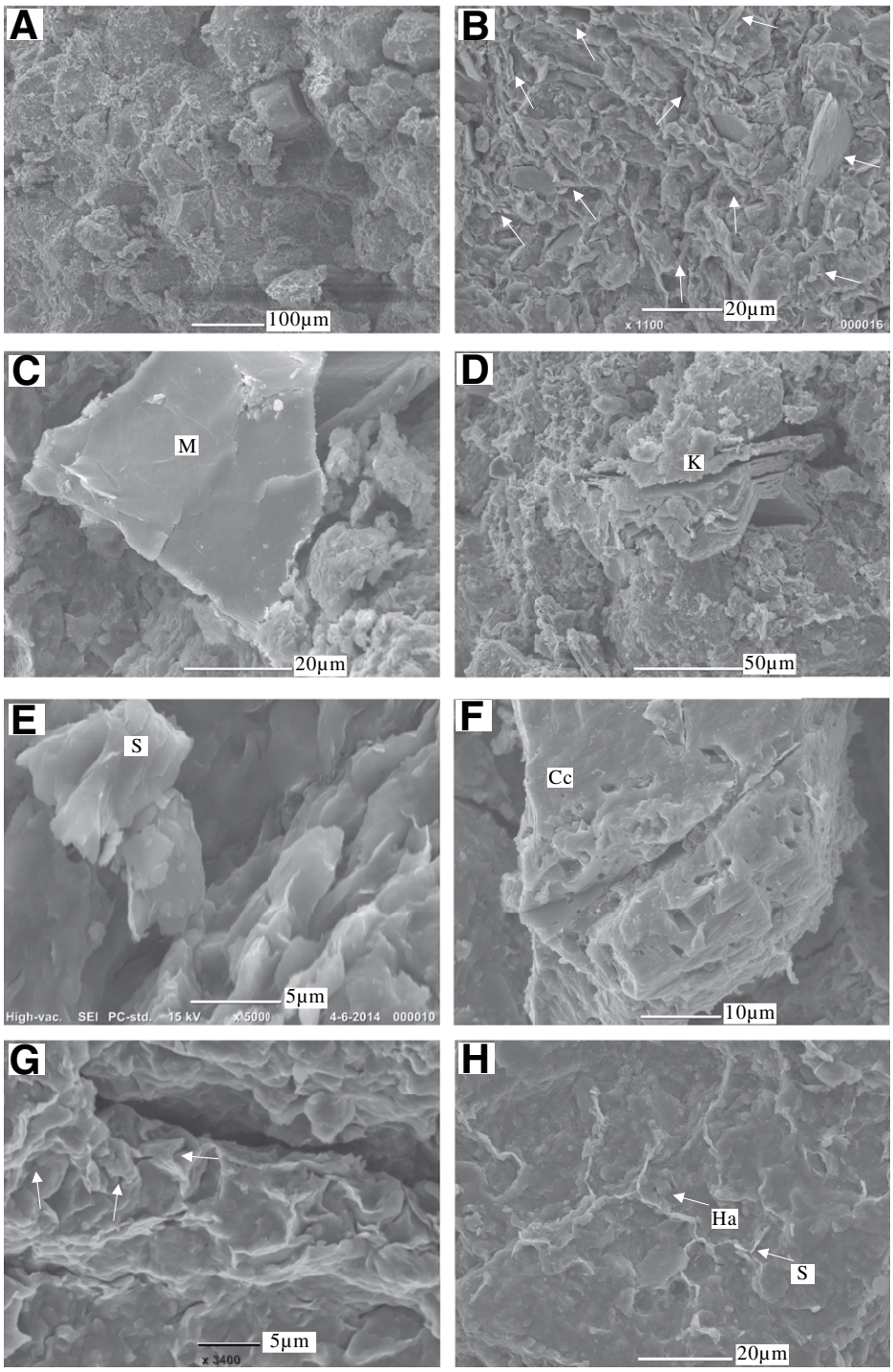

Figure 6. Examples of scanning electron microscope images showing morphology of clay and nonclay minerals in alluvial sandy and clayey mudstones. (A) Detrital particles showing subangular to well-rounded shape with matrix-support; clay particles cover the surface of detrital particles or occur as infill between detrital particles. (B) Detrital clay minerals showing thin platy morphology and random arrangement directions (white arrow). (C) Subangular detrital mica (M) particle. (D) Booklet-shaped detrital kaolinite (K) particle. (E) Inherited smectite (S) showing curled thin flakes with embayed edges. (F) Subrounded morphology and dissolved surface of calcite (Cc). (G) Clay mineral showing dissolution. (H) Cubic halite (Ha) present together with smectite in honeycomb and flake shape (S).

minerals are mostly less than 2 µm. Cubic halite forms together with these smectites (Fig. 6H), while it is rare in pedogenic sediments.

Clay Mineral Composition

Clay mineral assemblages <2 µm are composed of on average 64% smectite (ranging 50%–83%), 23% mixed-layer illite-smectite (7%–38%), 7% kaolinite (4%–16%), 4% illite (0%–10%), and 2% chlorite (0%–10%; Fig. 7; Table DR3 [see footnote 1]). Clay mineral analyses of the <0.2 µm size fractions of eight samples show a dominance of 85% smectite and 13% mixed-layer illite-smectite in this size fraction, with minor amounts of kaolinite (Table DR1 [see footnote 1]). Illite and chlorite are absent in the <0.2 µm size fractions.

Impact of Grain Size

Smectite and kaolinite reveal a decrease in abundance with decreasing grain size by 6.6% ($p = 0.0025$) and 3.9% ($p = 0.0000$) on average (Fig. 8A; Table DR2 [see footnote 1]), respectively, from sandy mudstones to clayey mudstones that show no postdepositional soil formation. In clayey mudstones, smectite abundance decreases with decreasing grain size by 8% ($p = 0.0325$) from clayey silt to clay samples, while kaolinite shows no remarkable change in the same samples (Fig. 8B, Table DR2 [see footnote 1]). Mixed-layer illite-smectite increases with decreasing grain size by 12.4% ($p = 0.0004$) from sandy mudstone to the finest clay samples (Fig. 8B; Table DR2 [see footnote 1]). The standard deviations of the mineral abundances indicate a large variety also within these groups, while all the data show significant changes at a confidence level of 95%. The other clay species, illite and chlorite, show no remarkable change dependent on grain size.

Impact of Soil Development

Clay mineral distributions of sediments with medium and intense soil development (SDI > 1) were compared in the same grain-size classes. In clayey mudstones, the proportion of smectite increases by 2.5% ($p = 0.1308$) on average from no or limited to medium and intense pedogenic samples (Fig. 8C; Table DR2 [see footnote 1]). The pedogenic increase of smectite spans 1%–3.5%, gradually increasing from clayey silt to clay samples (Fig. 8D; Table DR2 [see footnote 1]). Mixed-layer illite-smectite shows an opposite tendency compared to smectite. The mixed-layer illite-smectite decreases by 1.3% ($p = 0.4488$; Fig. 8C; Table DR2 [see footnote 1]) on average from no-or-limited to medium-and-intense pedogenesis and decreases by up to 3.1% in intense pedogenic samples

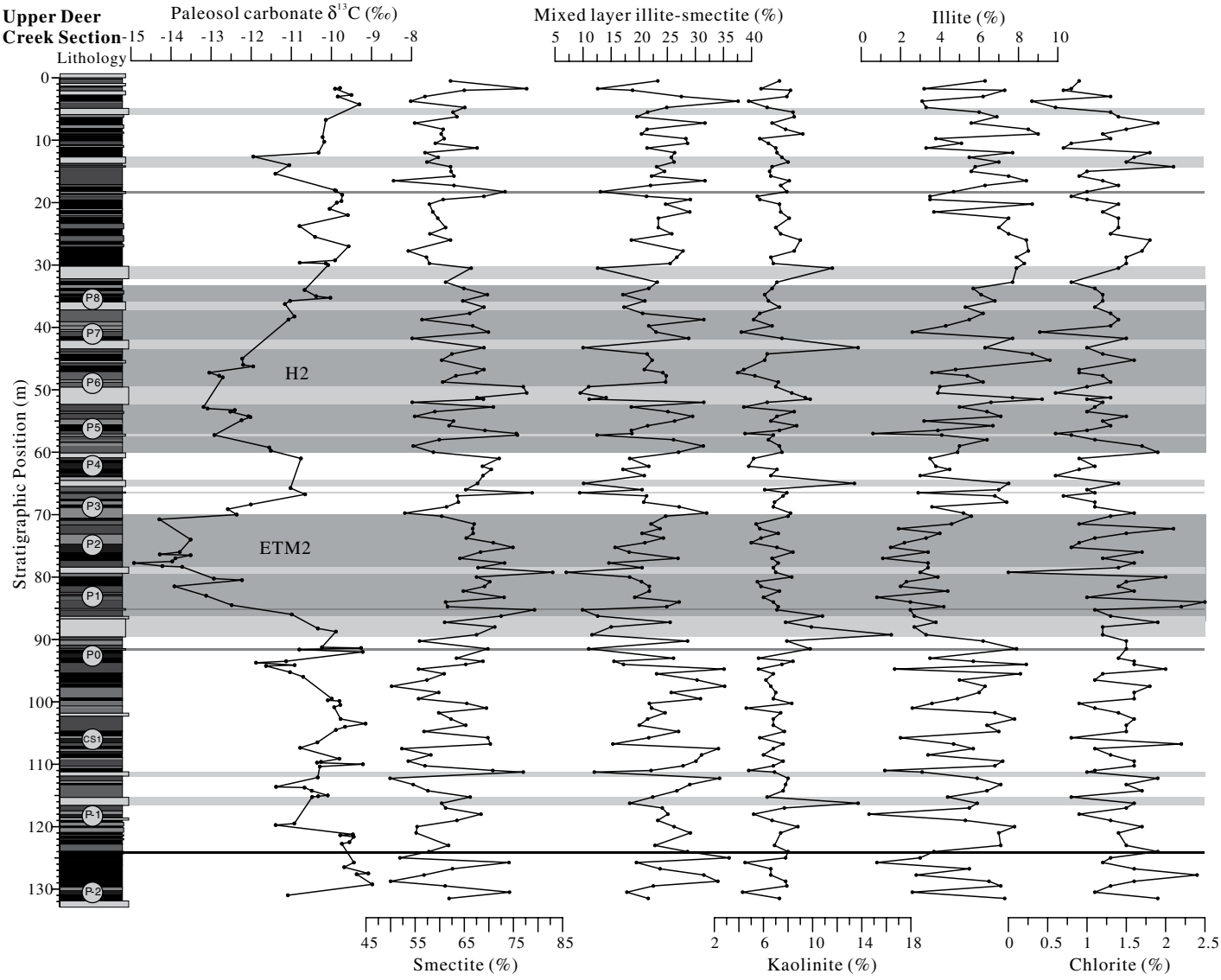

Figure 7. Clay mineral proportions of sediments in <2 µm fractions along the Upper Deer Creek (UDC) section. Records of paleosol carbonate $\delta^{13}C$ are indicated in the first column (Abels et al., 2012). Kaolinite is remarkably enriched in sands/silts, marked in tan bars, in which mixed-layer illite-smectite is lower. A significant increase of smectite is observed in the Eocene Thermal Maximum 2 (ETM2) and H2 (marked in gray bars), with decreases of mixed-layer illite-smectite and illite. The increment of smectite in the Eocene Thermal Maximum 2 is larger than that in the H2.

(Fig. 8D; Table DR2 [see footnote 1]). The decrease and increase of smectite and mixed-layer illite-smectite, respectively, from coarser to finer sediments could be caused by grain-size distribution (Fig. 8B; Table DR2 [see footnote 1]), while their changes from no-or-limited to medium-and-intense pedogenic samples are the result of pedogenesis. Illite and chlorite show an overall decrease with increasing pedogenesis, and kaolinite shows an increasing trend, albeit very small. The ANOVA showed no significant changes of clay proportions at a confidence level of 95% during soil development. Down soil profiles, clay minerals show roughly similar but even weaker trends as are seen with increasing soil development (Figure DR3 [see footnote 1]).

Impact of Eocene Thermal Maximum 2 and H2 Hyperthermals

The Eocene Thermal Maximum 2 (H1) and H2 have been recorded by a negative $\delta^{13}C$ excursion in the studied Upper Deer Creek section (Abels et al., 2012). We tested whether these hyperthermal events had impacts on the fluvial detrital input via erosion and/or hinterland rock weathering or subsequent weathering during pedogenesis. The bulk and clay mineralogy, sediment petrography, and grain-size signatures were evaluated against the stratigraphic occurrence of these hyperthermal events.

No significant changes in the mean grain size and bulk mineral composition were observed during the Eocene Thermal Maximum 2 or H2 hyperthermal events (Fig. 5; Tables DR1 and DR2 [see footnote 1]).

Clay mineral distributions from hyperthermals were also binned between samples showing no or limited postdepositional pedogenesis and samples showing medium and intense

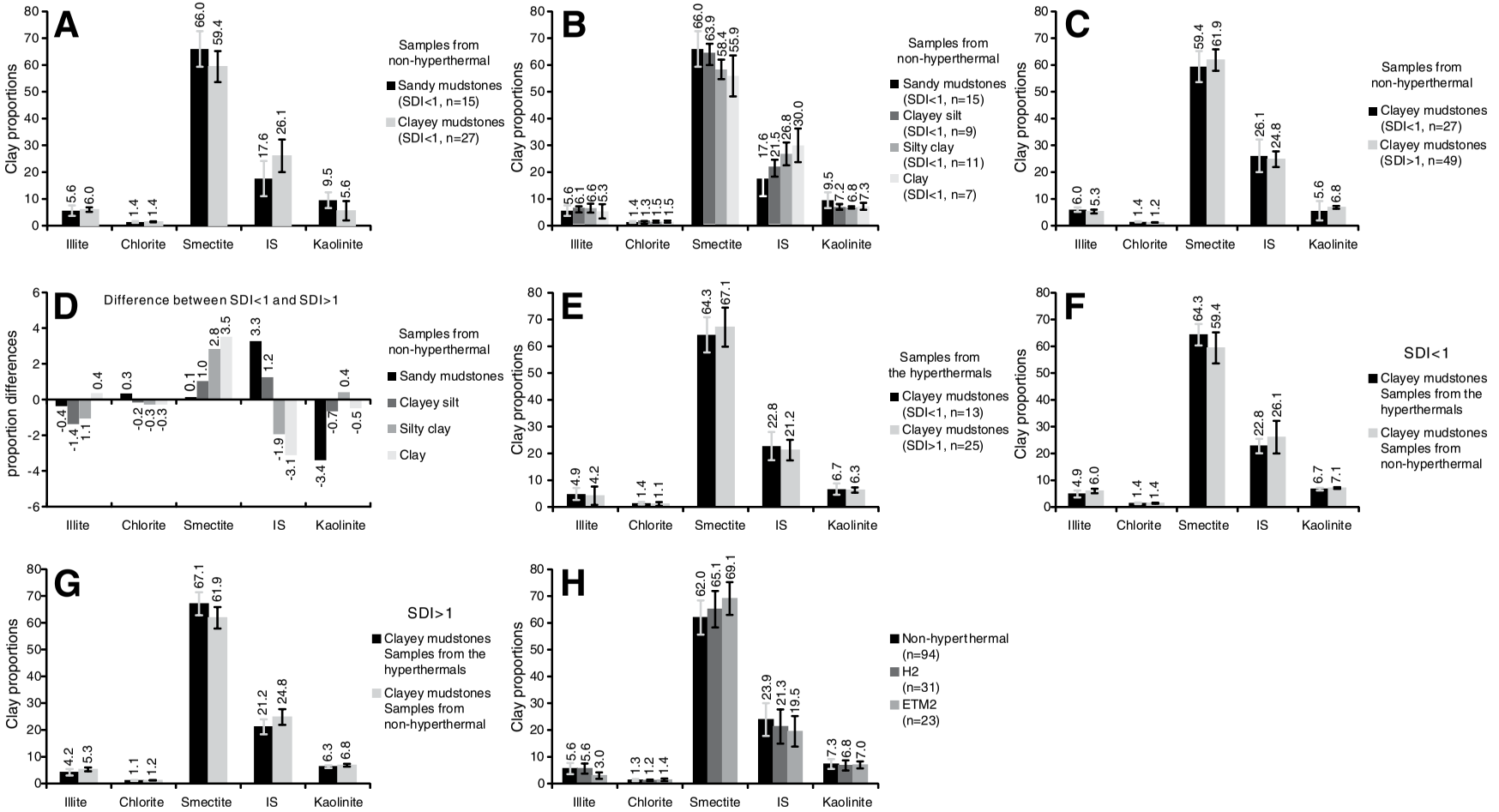

Figure 8. Average clay mineral distribution (<2 µm) in different grain-size classes and soil development index (SDI) from samples during and outside the hyperthermals. (A–B) Samples from sediments with no or limited soil development and non-hyperthermal sediments showing on average a decreasing trend of smectite and increasing trend of mixed-layer illite-smectite (IS) dependent on grain size. (C–D) Samples from non-hyperthermal sediments with different SDI values indicating on average slightly increasing smectite and kaolinite and decreasing mixed-layer illite-smectite dependent on soil formation (C) and few differences of clay mineral proportion in all grain-size classes (D). (E) Samples from hyperthermal sediments with different SDI values showing on average slightly increasing smectite and decreasing mixed-layer illite-smectite dependent on soil formation. (F–G) Samples from hyperthermal and non-hyperthermal sediments with different SDI values reflecting both increasing detrital smectite in sediments with no or limited soil development (F) and medium to intense soil development (G) dependent on hyperthermal. (H) Samples from non-hyperthermal, Eocene Thermal Maximum 2 (ETM2), and H2 sediments showing higher smectite and lower mixed-layer illite-smectite in hyperthermal sediments with respect to non-hyperthermal sediments. Line with bars represent the standard deviation.

pedogenesis. We defined a sample as being from a hyperthermal if the ongoing soil nodules depicted $\delta^{13}C$ values lower than −12‰ (Abels et al., 2012). Soil formation during the hyperthermal events showed an increase of smectite proportions of ~2.8% (p = 0.3853; Fig. 8E; Table DR2 [see footnote 1]), which is close to the ~2.5% increase found for soil formation outside the hyperthermals. The soil development in hyperthermals showed no significant clay mineralogical changes at a 95% confidence level, similar to outside the hyperthermals. The proportions of smectite showing pedogenesis and no pedogenesis were, however, on average ~4.9% (p = 0.0388; Fig. 8F; Table DR2 [see footnote 1]) and 5.3% (p = 0.0057; Fig. 8G; Table DR2 [see footnote 1]) higher in the hyperthermals ($\delta^{13}C > -12‰$) than outside the hyperthermals ($\delta^{13}C < -12‰$). Mixed-layer illite-smectite and illite on the other hand decreased respectively by 1.1% and 3.3%–3.6% in the detrital samples in the hyperthermals compared to those outside the hyperthermals. Changes of kaolinite and chlorite were negligible.

Clay mineral distributions in the individual hyperthermals (Eocene Thermal Maximum 2 and H2) were classified to test the magnitude of clay mineral changes caused by hyperthermals compared to those by non-hyperthermals (Table DR3 [see footnote 1]). Smectite increased by 7.1% (p = 0.0000) and 3.1% (p = 0.0213) in Eocene Thermal Maximum 2 and H2, respectively (Fig. 8H; Table DR2 [see footnote 1]). In contrast, mixed-layer illite-smectite, illite, and kaolinite were lower in Eocene Thermal Maximum 2 and H2 intervals.

DISCUSSION

Provenance of Willwood Formation Sediments

The detrital sediments in the Willwood Formation seem to be a homogeneous mixture of sedimentary rocks of Paleozoic, Mesozoic, and Paleocene age and igneous and metamorphic rocks (Neasham and Vondra, 1972). The Absaroka, Owl Creek, and Bighorn Mountains are the likely the main sources for these sediments, in line with paleocurrent data (Neasham and Vondra, 1972), while in the northern basin studied here in the McCullough Peaks area, the Beartooth Mountains could be an additional important source (Fig. 1). The subrounded morphologies of single calcite crystals and most quartz and feldspar grains in the McCoullough Peaks area suggest a nearby source. This is consistent with dolostone and limestone fragments found along the Absaroka Mountains in Willwood conglomerate beds indicating detrital products of proximal sources (Neasham and Vondra, 1972).

Diagenesis does not seem to have affected the clay mineral proportions in the Bighorn Basin Willwood Formation sediments. This can be derived from the relatively loose texture of the sediments and XRD results showing discrete clay minerals, kaolinite, illite, smectite, and chlorite, while ordered mixed-layered illite-smectite is not observed. The limited impact of diagenesis is consistent with previous clay mineralogical analysis and iron oxides analysis (Bao et al., 1998, 1999; Kraus and Hasiotis, 2006).

Clay aggregation morphologies in the alluvial sandstones point to a dominantly detrital origin. This includes the loose texture and randomly arranged direction of clay minerals, a thin platy morphology, the subangular shape of mica, the booklet-shaped debris with crooked plate morphology of kaolinite, and the sheet-like appearance with crumpled and embayed edges of smectite (Figs. 6B, 6C, and 6D; Wang et al., 2013). The detrital origin can be supported by the lack of significant proportional changes during postdepositional soil formation and fewer authigenic clay minerals being observed in sandy and clayey mudstones. The sediments in the study area seem to be a homogeneous mixture of different source rocks. This requires a smectite source much richer in smectite than the average of 64% detrital smectite content found in the Willwood Formation in the <2 μm fraction. Such a source is likely from reworked sediments that had hinterland detritus, volcanic sources, and pedogenically altered rocks rich in smectite. Cretaceous bentonites, such as SWy-2 in Wyoming, for example, may contain up to 75% smectite (Elzea and Murray, 1990; Chipera and Bish, 2001; Moll, 2001) and ~95% smectite in the <2 μm fraction and thus could be one of the potential sources. Clay mineralogy through the basin and of pre-Eocene sediments needs to be investigated to trace the distribution and provenance of the detrital smectite. Furthermore, continuous recycling of sediments in soils from the catchment and within the basin can also cause stepwise enrichment in smectite in detrital sediments as new formation of smectite occurred during pedogenesis.

Grain-Size Dependence of Clay Mineral Distributions

The clay mineralogy of the Willwood floodplains in the McCullough Peaks area shows grain-size dependence. The smectite and kaolinite proportions are higher and the illite-smectite proportions are lower in the sandy mudstones with respect to the clayey mudstones, which show no or limited pedogenesis (Figs. 8A and 8B). This points to different clay mineralogy between the depositional mechanisms responsible for the coarser and the finer deposits.

Most of the sandy deposits relate to (distal) crevasse-splay deposits, often within thicker avulsion belt deposits (Kraus and Gwinn, 1997) during the so-called avulsion phase (Abels et al., 2013). The finer deposits are brought to the floodplains during overbank flooding, representing the so-called overbank phase (Abels et al., 2013). The ~7-m-thick overbank-avulsion cycles are postulated to have been driven by precession-forced climate change, and the clay mineral changes between these facies could have been caused by precession-scale climate change in the hinterland. However, the sediments related to the avulsion phase were likely rapidly accumulated during river crevassing and avulsion, possibly within 1–2 k.y. (Morozova and Smith, 2000; Farrell, 2001; Abels et al., 2013). This duration is only 5%–10% of the 21 k.y. precession cycle, and climate change for weathering related to it is not likely to have been the main origin of the grain-size dependence of the clay mineralogy. In fact, a time duration of 1–2 k.y. for weathering of silicate minerals is two to four orders of magnitude slower than laboratory-derived rates for chemical weathering (White et al., 1996), which indicate that at least several thousand years of reaction time would be required, for instance, for plagioclase kaolinization (White and Brantley, 2003).

Alternatively, grain-size sorting could cause different clay mineralogies between sandy and clayey mudstones, as the mineral distribution in suspended matter depends mainly on the average size of hydrodynamical forces and surface electrochemical characteristics of the different species (Chamley, 1989). The higher occurrence of kaolinite in sandy lithologies is mainly caused by, first, large grains of kaolinite, which are mostly present in the sandy mudstones (Fig. 6C), while in the finest lithologies, detrital kaolinite particles are smaller (Table DR2 [see footnote 1]). This can be supported by our SEM observation that large kaolinite particles occur as aggregates in the sandy mudstones (Fig. 6D). Second, the kaolinite would preferentially settle because of its low surface electrochemical and less flocculated characteristics (Chamley, 1989). The size distribution of kaolinite in the Amazon and Mississippi Rivers shows that it had a range of 10–0.4 μm, peaking at 1–2 μm (Gibbs, 1977; Johnson and Kelley, 1984). In the <2 μm clay fraction of the Bighorn Basin samples, it is reasonable that kaolinite is rich in sandy mudstone and depleted in clayey mudstone, as suspended kaolinite with large grains (1–2 μm) might be transported much more slowly than much smaller grains and would settle mainly in sandy

mudstone but rarely in clayey mudstone (Inglès and Ramos-Guerrero, 1995). Kaolinite is rare in the clay fractions <0.2 μm, which could be the result of kaolinite being rare in this grain-size class in the source areas (Table DR2 [see footnote 1]). The impact of neoformation during pedogenesis is likely negligible, as only a slight change in kaolinite is observed (Fig. 8C). If grain-size sorting caused the differences in kaolinite, a clay mineral distribution transect from basin margin to basin center should show a strong trend of coarse-grained kaolinite along the margins to fine-grained kaolinite in the center.

Smectite differences between coarser-grained and finer-grained sediments could mainly be the result of the aggregated particle size. In general, suspended smectite is of small grain size (<1 μm) and preferentially floats in the river because its flake shape and electrochemical characteristics dominate (Chamley, 1989; Konta, 1985). The large decrease by 11% of smectite from coarser-grained to finer-grained sediments could be explained by larger floods bringing in coarser-grained sediments, which may contain more smectite during the avulsion phases or crevasse-splay events, than by regular overbank floods. We hypothesize that larger floods that more often result in crevassing and avulsion of channels cause less hydrodynamical sorting and more soil erosion. Less hydrodynamical sorting would lead to a mixture of both coarse and finer (<0.2 μm) grains, which are rich in smectite (Table DR2 [see footnote 1]). Eroded soils, such as preexisting floodplain paleosols, are relatively rich in smectite, as shown by the increase in smectite due to pedogenesis in our data (Figs. 6H, 8C,and 8E). In the floodplain facies, river flow could have transported the floating smectite downstream with less eroded smectite inputs, leading to lower smectite contents.

Clay Mineral Neoformation during Pedogenesis

The smectite in the Willwood Formation paleosols shows curled, thin flakes on the surface of flat clay plates (Fig. 6E) that could be either inherited smectite or transformed products from older weathering phases. Some smectites were observed with incipient honeycomb shapes (Fig. 6H), however, pointing to an authigenic origin due to neoformation. The neoformed smectite possibly precipitated from pore water associated with seasonal changes of groundwater tables (Worden and Morad, 2003; Raigemborn et al., 2014). Neoformation of smectite in the Willwood paleosols is consistent with a slight increase in smectite down into soil profiles (Figure DR3 [see footnote 1]) and with increasing pedogenesis (Figs. 8C and 8E), though on average, the observed increases in smectite are not significantly different from background values. Both of these, however, show weak trends, likely because of the dominance of detrital clay minerals and the relatively short time available for soil development after deposition due to the relatively high sedimentation rates in the McCullough Peaks floodplains (on average 0.34 mm/yr or 34 cm/k.y.; Abels et al., 2016). An individual soil has a formation time of hundreds to several thousands of years (Abels et al., 2013), and less than the more than tens of thousands of years needed for a significant impact of chemical weathering (White et al., 1996).

Neoformation of smectite occurs commonly at intermediate depths in weathering profiles under temperate to warm-subarid conditions (Chamley, 1989; Šucha et al., 2001). The increase in smectite and decreases in mixed-layer illite-smectite and illite along the individual vertical soil horizons, and with increasing soil formation, suggest that the neoformation of smectite occurred at the cost of mixed-layer illite-smectite and illite (Figure DR3 [see footnote 1]). Clays showing dissolved surface morphology are found in the clayey mudstones, supporting the suggestion that these were derived from illite and/or mixed-layer illite-smectite (Figure DR1a and 1b [see footnote 1]). This was confirmed by elemental composition analysis, as the dissolved minerals rich in K could be illite (Figure DR2c and 2e [see footnote 1]) and those rich in Mg and minor K could be mixed-layer illite-smectite (Figure DR2d and 2f [see footnote 1]). Vertisols, which are the common soil types in the Bighorn Basin (Kraus and Aslan, 1993), usually show decreases in illite and increases in smectite with increasing pedogenesis (Graham and Southard, 1983; Badraoui and Bloom, 1990). As mixed-layer illite-smectite is much more dominant than illite, mixed-layer illite-smectite is likely to be the main source of neoformed smectite. Illite may also contribute to smectite formation, especially in the soil B horizons, where illite decreases significantly (Figure DR3 [see footnote 1]).

The neoformation of smectite occurs under specific conditions. Generally, subtropical climates, a well-marked dry season, and poorly drained, high pH conditions, where Si, Al, and Fe tend to accumulate, are favored (Chamley, 1989; Wilson, 1999; Bühmann and Schoeman, 1995). Well-developed slickensides, carbonate nodules, iron-oxide mottling, purple paleosols, and ichnofossil assemblages in paleosols in the studied early Eocene sections support seasonally wet and dry climates as well as poorly drained conditions (e.g., Kraus and Aslan, 1993; Kraus and Riggins, 2007; Smith et al., 2008). During the wet season, ions were released from minerals in line with mineral dissolution features visible on SEM images (Figs. 6F and 6G). These minerals, likely illite, chlorite, calcite, mixed-layer illite-smectite, and possibly dolomite, provided Si, Fe, Mg, Ca, Na, and sometimes Al ions. The ions subsequently leached and concentrated in the soil B horizons of the Vertisols during the dry season. These elements formed new minerals such as smectite. Excess Ca and Fe in the soil B horizons formed the carbonate nodules and iron-oxide mottling during the dry season. Previous studies documented poorly drained conditions in the early Eocene Bighorn Basin (e.g., Kraus and Aslan, 1993; Smith et al., 2008), with hydrolysis taking place in seasonally wet-dry conditions favoring the neoformation of smectite rather than kaolinite (Wilson, 1999). Low pH associated with organic acid in upper horizons favored the dissolution of calcite and provided the Ca for leaching downwards, as indicated in Figure 6F. The pH, however, increased downwards to alkaline values in the soil B horizon, facilitating the precipitation of Al and Fe and intensifying the activity of Si (Wilson, 1999).

Physical and Chemical Weathering during Eocene Thermal Maximum 2 and H2

The Eocene Thermal Maximum 2 (H1) and H2 greenhouse warming events caused an enhanced input of detrital clay minerals rather than increasing in situ soil weathering after deposition. Interestingly, the compositional changes caused by the changes in detrital clay are similar to the clay mineralogical changes that we observed during in situ soil formation during and outside the hyperthermal events (Figs. 8F and 8G). These are increasing amounts of smectite and decreasing amounts of illite-smectite and illite (Figs. 8F and 8G). A larger increase of detrital smectite was observed during Eocene Thermal Maximum 2 than during H2 (Table DR3 [see footnote 1]), which would be expected because the disturbance to the carbon cycle, and resulting climate impact of Eocene Thermal Maximum 2, was greater (Stap et al., 2010; Abels et al., 2016).

Cyclostratigraphic analysis of the Upper Deer Creek section has shown that the overbank-avulsion cycles have a similar thickness in the Eocene Thermal Maximum 2–H2 interval as before and after (Abels et al., 2012, 2013, 2016), suggesting no significant changes in local floodplain sedimentation rate occurred during the greenhouse warming events. Grain-size analysis and bulk mineral composition also do not show significant changes across the hyperthermal events in the Upper Deer Creek section (Fig. 5),

suggesting that the parent material for soil formation during Eocene Thermal Maximum 2 and H2 was similar as before and after. Since sedimentation rates and provenance remained similar during the events, enhanced smectite neoformation during soil formation in more proximal settings and reworking of these or preexisting smectite-rich sediments are the likely processes causing the observed increase in smectite.

We hypothesize that enhanced seasonal climates during Eocene Thermal Maximum 2 and H2 caused changes in the clay mineral assemblages of the Willwood Formation. First, enhanced climate seasonality might have caused enhanced erosion of proximal laterites and enhanced recycling of intrabasinal floodplain soils. Second, enhanced climate seasonality might have caused small increases in clay neoformation during soil formation, as we observed, which cumulatively could still significantly contribute to the observed clay mineralogical change. The Willwood Formation paleosols show abundant characteristics of predominantly seasonal climates, partially under poorly drained conditions, in the early Eocene Bighorn Basin (Kraus, 2002). The observed lack of authigenic kaolinite in general, as well as during the hyperthermal events, substantiates the seasonal character of the local climates. Greenhouse warming during the hyperthermals might have enhanced the climate seasonality, as is suggested for the Paleocene-Eocene Thermal Maximum (Foreman, 2014; Smith et al., 2008).

Enhanced climate seasonality resulting in oscillations in short-term precipitation could have caused a less dense vegetation cover, reducing the cohesiveness of overbank sediments and upstream laterites (Cancienne et al., 2008; Foreman, 2014, and the references therein). During the Paleocene-Eocene Thermal Maximum, evidence for increased bank erosion has been observed in the Bighorn Basin, likely related to oscillations in short-term precipitation and fluctuations in the water table (Foreman, 2014). Similar processes might have occurred during the younger hyperthermals, although the soil bulk oxide precipitation proxy (CALMAG) points to the opposite trend between the Paleocene-Eocene Thermal Maximum and Eocene Thermal Maximum 2 (Abels et al., 2016), which may suggest that climate was not impacted linearly. However, the CALMAG mean annual precipitation proxy is not a measure of precipitation seasonality, and the new clay mineralogical change seems to indicate that, similar to the Paleocene-Eocene Thermal Maximum, increased seasonality of precipitation occurred in the Bighorn Basin during Eocene Thermal Maximum 2.

Clechenko et al. (2007) reported high abundances of kaolinite in a weathering profile related to the Paleocene-Eocene Thermal Maximum in the Williston Basin, in the continental interior of the United States, 600 km to the northeast from the Bighorn Basin. The increase in kaolinite in the Williston Basin could only be related to intensified pedogenesis, as the sources to deliver these amounts of kaolinite are not known, while pre–Paleocene-Eocene Thermal Maximum intervals are dominated by smectite. These findings seem to be in strong contrast with the increase in smectite we found in the Bighorn Basin during the subsequent Eocene Thermal Maximum 2 event and the limited impact on clay mineralogy of intensified pedogenesis. This could mean that the Bighorn and Williston Basins had contrasting weathering impacts during the early Eocene hyperthermals or Paleocene-Eocene Thermal Maximum and Eocene Thermal Maximum 2 or that the local settings between the two basins were largely different.

CONCLUSION

Clay minerals of the Willwood Formation in the Upper Deer Creek section of the Bighorn Basin, Wyoming, are 64% (±7%) smectite and 23% (±6%) mixed-layer illite-smectite, with minor components of 7% (±2%) kaolinite, 5.2% (±2.1%) illite, and 1.7% (±0.4%) chlorite. Most clay minerals in Eocene soil profiles from Bighorn Basin floodplains are detrital in origin. The clay mineralogy differs between clastic grain-size classes, indicating that grain size has an impact on clay mineral distribution. Soil formation caused insignificant increases in smectite and insignificant decreases in mixed-layer illite-smectite and illite. This is consistent with the inferred seasonal character of early Eocene local climate. We hypothesize that the short time available for formation of individual soils of several thousands years at most caused the insignificant character of the clay mineral changes, consistent with long time scales over which chemical weathering is thought to act.

Two early Eocene hyperthermals, Eocene Thermal Maximum 2 and H2, caused similar changes as seen during in situ pedogenesis, with an increase in smectite and decreases in mixed-layer illite-smectite and illite. However, postdepositional in situ pedogenesis during the smaller hyperthermals caused only very small increases in smectite, indicating that most of the clay mineralogy changes were detrital in origin. We hypothesize that the small increases in smectite neoformation during in situ pedogenesis were again caused by the short time available during soil formation despite the likely considerable climate change during these hyperthermals. The fact that we still documented pedogenic-type clay mineral changes during these events could be related to enhanced erosion of preexisting soils in the catchment area and recycling of intrabasinal floodplain soils driven by enhanced climate seasonality.

These findings seem to contrast with the large increase in authigenic kaolinite observed in the nearby Williston Basin during the Paleocene-Eocene Thermal Maximum, which was interpreted as indicating intensification of chemical weathering during this hyperthermal event. For now, this could point to dissimilarity of weathering responses in the Williston and Bighorn Basins during the early Eocene hyperthermals due to climatic or geologic differences between the basins. Alternatively, it may point to dissimilar climatic responses of the Paleocene-Eocene Thermal Maximum and Eocene Thermal Maximum 2 events, as was recently suggested using the soil bulk oxide mean annual precipitation proxy, which showed contrasting precipitation regimes between the two events in the Bighorn Basin. Clearly, our results indicate additional studies are needed to improve our understanding of the terrestrial climate and weathering responses to past greenhouse warming episodes, as increased chemical weathering may act as a negative feedback mechanism to global warming.

ACKNOWLEDGMENTS

We thank Nancy Weyns and Ria Brepoels for laboratory assistance at Leuven University, Belgium; Gil Pennock, Wilma Wessels, and Ton Zalm for laboratory assistance at Utrecht University, Netherlands; and Frits Hilgen and Peter van den Berg for field assistance. We extend our gratitude also to *GSA Bulletin* Editors Bradley S. Singer and Benjamin J.C. Laabs for their editorial handling. We also acknowledge the constructive comments of two anonymous reviewers and Kathryn E. Snell. Wang thanks Zhaohui Li and Gordon J. Churchman for writing assistance. Abels acknowledges the Netherlands Organization for Scientific Research (NWO) Earth and Life Sciences (ALW) for a VENI grant (863.11.006). Wang is grateful for grants from the Chinese Scholarship Council (CSC), National Natural Science Youth Foundation of China (grant 41602037), Natural Science Youth Foundation of Hubei (grant 2016CFB183), the Postdoctoral Science Foundation of China (grant 2015M582301), and Fundamental Research Funds for the Central Universities, China University of Geosciences (Wuhan, CUG160848). The Department of Earth Sciences at Utrecht University, Netherlands, is thanked for hosting author Wang. The Chevron company is thanked for permission to use the SYBILLA software.

REFERENCES CITED

Abels, H.A., Clyde, W.C., Gingerich, P.D., Hilgen, F.J., Fricke, H.C., Bowen, G.J., and Lourens, L.J., 2012, Terrestrial carbon isotope excursions and biotic change during Palaeogene hyperthermals: Nature Geoscience, v. 5, p. 326–329, doi:10.1038/ngeo1427.

Abels, H.A., Kraus, M.J., and Gingerich, P.D., 2013, Precession-scale cyclicity in the fluvial lower Eocene Willwood Formation of the Bighorn Basin, Wyoming (USA): Sedimentology, v. 60, p. 1467–1483, doi:10.1111/sed.12039.

Abels, H.A., Lauretano, V., Van Yperen, A., Hopman, T., Zachos, J.C., Lourens, L.J., Gingerich, P.D., and Bowen, G.J., 2016, Environmental impact and magnitude of paleosol carbonate carbon isotope excursions marking five early Eocene hyperthermals in the Bighorn Basin, Wyoming: Climate of the Past, v. 12, p. 1151–1163, doi:10.5194/cp-12-1151-2016.

Badraoui, M., and Bloom, P.R., 1990, Iron-rich high-charge beidellite in Vertisols and Mollisols of the High Chaouia region of Morocco: Soil Science Society of America Journal, v. 54, p. 267–274, doi:10.2136/sssaj1990.03615995005400010043x.

Bains, S., Corfield, R.M., and Norris, R.D., 1999, Mechanisms of climate warming at the end of the Paleocene: Science, v. 285, p. 724–727, doi:10.1126/science.285.5428.724.

Bao, H., Koch, P.L., and Hepple, R.P., 1998, Hematite and calcite coatings on fossil vertebrates: Journal of Sedimentary Research, v. 68, p. 727–738, doi:10.2110/jsr.68.727.

Bao, H., Koch, P.L., and Rumble, D., 1999, Paleocene–Eocene climatic variation in western North America: Evidence from the $\delta^{18}O$ of pedogenic hematite: Geological Society of America Bulletin, v. 111, p. 1405–1415, doi:10.1130/0016-7606(1999)111<1405:PECVIW>2.3.CO;2.

Bolle, M., and Adatte, T., 2001, Palaeocene–early Eocene climatic evolution in the Tethyan realm: Clay mineral evidence: Clay Minerals, v. 36, p. 249–261, doi:10.1180/000985501750177979.

Bowen, G.J., and Bowen, B.B., 2008, Mechanisms of PETM global change constrained by a new record from central Utah: Geology, v. 36, p. 379–382, doi:10.1130/G24597A.1.

Bowen, G.J., and Zachos, J.C., 2010, Rapid carbon sequestration at the termination of the Palaeocene-Eocene Thermal Maximum: Nature Geoscience, v. 3, p. 866–869, doi:10.1038/ngeo1014.

Bown, T.M., and Kraus, M.J., 1987, Integration of channel and floodplain suites: I. Developmental sequence and lateral relations of alluvial paleosols: Journal of Sedimentary Petrology, v. 57, p. 587–601.

Bühmann, C., and Schoeman, J.L., 1995, A mineralogical characterization of Vertisols from the northern regions of the Republic of South Africa: Geoderma, v. 66, p. 239–257, doi:10.1016/0016-7061(94)00080-T.

Cancienne, R.M., Fox, G.A., and Simon, A., 2008, Influence of seepage undercutting on the stability of root-reinforced streambanks: Earth Surface Processes and Landforms, v. 33, p. 1769–1786, doi:10.1002/esp.1657.

Chamley, H., 1989, Clay Sedimentology: Berlin, Germany, Springer-Verlag, 623 p.

Chipera, S.J., and Bish, D.L., 2001, Baseline studies of the Clay Minerals Society source clays: Powder X-ray diffraction analyses: Clays and Clay Minerals, v. 49, p. 398–409, doi:10.1346/CCMN.2001.0490507.

Clechenko, E.R., Kelly, D.C., Harrington, G.J., and Stiles, C.A., 2007, Terrestrial records of a regional weathering profile at the Paleocene-Eocene boundary in the Williston Basin of North Dakota: Geological Society of America Bulletin, v. 119, p. 428–442, doi:10.1130/B26010.1.

Dickens, G.R., O' Neil, J.R., Rea, D.K., and Owen, R.M., 1995, Dissociation of oceanic methane hydrate as a cause of the carbon isotope excursion at the end of the Paleocene: Paleoceanography, v. 10, p. 965–971, doi:10.1029/95PA02087.

Dypvik, H., Riber, L., Burca, F., Rüther, D., Jargvoll, D., Nagy, J., and Jochmann, M., 2011, The Paleocene-Eocene Thermal Maximum (PETM) in Svalbard—Clay mineral and geochemical signals: Palaeogeography, Palaeoclimatology, Palaeoecology, v. 302, p. 156–169, doi:10.1016/j.palaeo.2010.12.025.

Elzea, J.M., and Murray, H.H., 1990, Variation in the mineralogical, chemical and physical properties of the Cretaceous Clay Spur bentonite in Wyoming and Montana (USA): Applied Clay Science, v. 5, p. 229–248, doi:10.1016/0169-1317(90)90012-E.

Ernst, S.R., Guasti, E., Dupuis, C., and Speijer, R.P., 2006, Environmental perturbation in the southern Tethys across the Paleocene/Eocene boundary (Dababiya, Egypt): Foraminiferal and clay mineral records: Marine Micropaleontology, v. 60, p. 89–111, doi:10.1016/j.marmicro.2006.03.002.

Fanshawe, J.R., 1971, Structural evolution of Bighorn Basin, *in* Renfro, et al., eds., Symposium on Wyoming Tectonics and their Economic Significance; 23rd Annual Field Conference Guidebook: Casper, Wyoming Geological Association, p. 35–37.

Farrell, K.M., 2001, Geomorphology, facies architecture, and high-resolution, non-marine sequence stratigraphy in avulsion deposits, Cumberland Marshes, Saskatchewan: Sedimentary Geology, v. 139, p. 93–150, doi:10.1016/S0037-0738(00)00150-0.

Foreman, B.Z., 2014, Climate-driven generation of a fluvial sheet sand body at the Paleocene-Eocene boundary in north-west Wyoming (USA): Basin Research, v. 26, p. 225–241, doi:10.1111/bre.12027.

Foreman, B.Z., Heller, P.L., and Clementz, M.T., 2012, Fluvial response to abrupt global warming at the Palaeocene/Eocene boundary: Nature, v. 491, p. 92–95, doi:10.1038/nature11513.

Gibbs, R.J., 1977, Transport phases of transition metals in the Amazon and Yukon Rivers: Geological Society of America Bulletin, v. 88, p. 829–843, doi:10.1130/0016-7606(1977)88<829:TPOTMI>2.0.CO;2.

Gibson, T.G., Bybell, L.M., and Mason, D.B., 2000, Stratigraphic and climatic implications of clay mineral changes around the Paleocene/Eocene boundary of the northeastern U.S. margin: Sedimentary Geology, v. 134, p. 65–92, doi:10.1016/S0037-0738(00)00014-2.

Graham, R.C., and Southard, A.R., 1983, Genesis of a Vertisol and an associated Mollisol in northern Utah: Soil Science Society of America Journal, v. 47, p. 552–559, doi:10.2136/sssaj1983.03615995004700030032x.

Inglès, M., and Ramos-Guerrero, E., 1995, Sedimentological control on the clay mineral distribution in the marine and non-marine Palaeogene deposits of Mallorca (Western Mediterranean): Sedimentary Geology, v. 94, p. 229–243, doi:10.1016/0037-0738(94)00089-D.

Jackson, M.L., 1975, Soil Chemical Analysis Advanced Course (2nd ed.): Madison, Wisconsin, M.L. Jackson, 895 p.

John, C.M., Banerjee, N.R., Longstaffe, F.J., Sica, C., Law, K.R., and Zachos, J.C., 2012, Clay assemblage and oxygen isotopic constraints on the weathering response to the Paleocene-Eocene Thermal Maximum, east coast of North America: Geology, v. 40, p. 591–594, doi:10.1130/G32785.1.

Johnson, L.R., and Kelley, J.T., 1984, Temporal, spatial, and texture variation in the mineralogy of Mississippi River suspended sediment: Journal of Sedimentary Petrology, v. 54, p. 67–72.

Konta, J., 1985, Crystalline minerals and chemical maturity of suspended matter in major rivers sample sunder the SCOPE/UNEP project: Mineralology and Petrology Acta, v. 29A, p. 121–133.

Kraus, M.J., 2002, Basin-scale changes in floodplain paleosols: Implications for interpreting alluvial architecture: Journal of Sedimentary Research, v. 72, p. 500–509, doi:10.1306/121701720500.

Kraus, M.J., and Aslan, A., 1993, Eocene hydromorphic paleosols; significance for interpreting ancient floodplain processes: Journal of Sedimentary Research, v. 63, p. 453–463.

Kraus, M.J., and Gwinn, B., 1997, Facies and facies architecture of Paleogene floodplain deposits, Willwood Formation, Bighorn Basin, Wyoming, USA: Sedimentary Geology, v. 114, p. 33–54, doi:10.1016/S0037-0738(97)00083-3.

Kraus, M.J., and Hasiotis, S.T., 2006, Significance of different modes of rhizolith preservation to interpreting paleoenvironmental and paleohydrologic settings: Examples from Paleogene paleosols, Bighorn Basin, Wyoming, U.S.A.: Journal of Sedimentary Research, v. 76, p. 633–646, doi:10.2110/jsr.2006.052.

Kraus, M.J., and Riggins, S., 2007, Transient drying during the Paleocene-Eocene Thermal Maximum (PETM): Analysis of paleosols in the Bighorn Basin, Wyoming: Palaeogeography, Palaeoclimatology, Palaeoecology, v. 245, p. 444–461, doi:10.1016/j.palaeo.2006.09.011.

Kraus, M.J., McInerney, F.A., Wing, S.L., Secord, R., Baczynski, A.A., and Bloch, J.I., 2013, Paleohydrologic response to continental warming during the Paleocene-Eocene Thermal Maximum, Bighorn Basin, Wyoming: Palaeogeography, Palaeoclimatology, Palaeoecology, v. 370, p. 196–208, doi:10.1016/j.palaeo.2012.12.008.

Kump, L.R., Brantley, S.L., and Arthur, M.A., 2000, Chemical weathering, atmospheric CO_2, and climate: Annual Review of Earth and Planetary Sciences, v. 28, p. 611–667, doi:10.1146/annurev.earth.28.1.611.

Kurtz, A.C., Kump, L.R., Arthur, M.A., Zachos, J.C., and Paytan, A., 2003, Early Cenozoic decoupling of the global carbon and sulfur cycles: Paleoceanography, v. 18, p. 1090, doi:10.1029/2003PA000908.

Lauretano, V., Littler, K., Polling, M., Zachos, J.C., and Lourens, L.J., 2015, Frequency, magnitude and character of hyperthermal events at the onset of the early Eocene climatic optimum: Climate of the Past, v. 11, p. 1313–1324, doi:10.5194/cp-11-1313-2015.

Lourens, L.J., Sluijs, A., Kroon, D., Zachos, J.C., Thomas, E., Röhl, U., Bowles, J., and Raffi, I., 2005, Astronomical pacing of late Palaeocene to early Eocene global warming events: Nature, v. 435, p. 1083–1087, doi:10.1038/nature03814.

Maas, M.C., Anthony, M.R., Gingerich, P.D., Gunnell, G.F., and Krause, D.W., 1995, Mammalian generic diversity and turnover in the late Paleocene and early Eocene of the Bighorn and Crazy Mountains Basins, Wyoming and Montana (USA): Palaeogeography, Palaeoclimatology, Palaeoecology, v. 115, p. 181–207, doi:10.1016/0031-0182(94)00111-K.

McInerney, F.A., and Wing, S.L., 2011, The Paleocene-Eocene Thermal Maximum: A perturbation of carbon cycle, climate, and biosphere with implications for the future: Annual Review of Earth and Planetary Sciences, v. 39, p. 489–516, doi:10.1146/annurev-earth-040610-133431.

Moll, W.F., Jr., 2001, Baseline studies of the Clay Minerals Society source clays: Geological origin: Clays and Clay Minerals, v. 49, p. 374–380, doi:10.1346/CCMN.2001.0490503.

Morozova, G.S., and Smith, N.D., 2000, Holocene avulsion styles and sedimentation patterns of the Saskatchewan River, Cumberland Marshes, Canada: Sedimentary Geology, v. 130, p. 81–105, doi:10.1016/S0037-0738(99)00106-2.

Neasham, J.W., and Vondra, C.F., 1972, Stratigraphy and petrology of the lower Eocene Willwood Formation, Bighorn Basin, Wyoming: Geological Society of America Bulletin, v.83,p.2167–2180,doi:10.1130/0016-7606(1972)83[2167:SAPOTL]2.0.CO;2.

Nicolo, M.J., Dickens, G.R., Hollis, C.J., and Zachos, J.C., 2007, Multiple early Eocene hyperthermals: Their sedimentary expression on the New Zealand continental margin and in the deep sea: Geology, v. 35, p. 699–702, doi:10.1130/G23648A.1.

Oyama, M., and Takehara, H., 1970, Revised Standard Soil Color Charts: Tokyo, Japan, Research Council for Agriculture, Forestry, and Fisheries, 27 p.

Raigemborn, M.S., Gómez-Peral, L.E., Krause, J.M., and Matheos, S.D., 2014, Controls on clay minerals assemblages in an early Paleogene nonmarine succession: Implications for the volcanic and paleoclimatic record of extra-Andean Patagonia, Argentina: Journal of South American Earth Sciences, v. 52, p. 1–23, doi:10.1016/j.jsames.2014.02.001.

Robert, C., and Kennett, J.P., 1994, Antarctic subtropical humid episode at the Paleocene-Eocene boundary: Clay-mineral evidence: Geology, v. 22, p. 211–214, doi:10.1130/0091-7613(1994)022<0211:ASHEAT>2.3.CO;2.

Sakharov, B.A., Lindgreen, H., Salyn, A., and Drits, V.A., 1999, Determination of illite-smectite structures using multispecimen X-ray diffraction profile fitting: Clays and Clay Minerals, v. 47, p. 555–566, doi:10.1346/CCMN.1999.0470502.

Sluijs, A., Röhl, U., Schouten, S., Brumsack, H.J., Sangiorgi, F., Sinninghe Damsté, J.S., and Brinkhuis, H., 2008, Arctic late Paleocene–early Eocene paleoenvironments with special emphasis on the Paleocene-Eocene Thermal Maximum (Lomonosov Ridge, Integrated Ocean Drilling Program Expedition 302): Paleoceanography, v. 23, p. PAS11, doi:10.1029/2007PA001495.

Sluijs, A., Schouten, S., Donders, T.H., Schoon, P.L., Röhl, U., Reichart, G., Sangiorgi, F., Kim, J., Sinninghe Damsté, J.S., and Brinkhuis, H., 2009, Warm and wet conditions in the Arctic region during Eocene Thermal Maximum 2: Nature Geoscience, v. 2, p. 777–780, doi:10.1038/ngeo668.

Smith, J.J., Hasiotis, S.T., Kraus, M.J., and Woody, D.T., 2008, *Naktodemasis bowni*: New ichnogenus and ichnospecies for adhesive meniscate burrows (AMB), and paleoenvironmental implications, Paleogene Willwood Formation, Bighorn Basin, Wyoming: Journal of Paleontology, v. 82, p. 267–278, doi:10.1666/06-023.1.

Soliman, M.F., Aubry, M., Schmitz, B., and Sherrell, R.M., 2011, Enhanced coastal paleoproductivity and nutrient supply in Upper Egypt during the Paleocene/Eocene Thermal Maximum (PETM): Mineralogical and geochemical evidence: Palaeogeography, Palaeoclimatology, Palaeoecology, v. 310, p. 365–377, doi:10.1016/j.palaeo.2011.07.027.

Środoń, J., Drits, V.A., McCarty, D.K., Hsieh, J.C.C., and Eberl, D.D., 2001, Quantitative X-ray diffraction analysis of clay-bearing rocks from random preparations: Clays and Clay Minerals, v. 49, p. 514–528, doi:10.1346/CCMN.2001.0490604.

Stap, L., Sluijs, A., Thomas, E., and Lourens, L., 2009, Patterns and magnitude of deep sea carbonate dissolution during Eocene Thermal Maximum 2 and H2, Walvis Ridge, southeastern Atlantic Ocean: Paleoceanography, v. 24, p. PA1211, doi:10.1029/2008PA001655.

Stap, L., Lourens, L.J., Thomas, E., Sluijs, A., Bohaty, S., and Zachos, J.C., 2010, High-resolution deep-sea carbon and oxygen isotope records of Eocene Thermal Maximum 2 and H2: Geology, v. 38, p. 607–610, doi:10.1130/G30777.1.

Šucha, V., Środoń, J., Clauer, N., Elsass, F., Eberl, D.D., Kraus, I., and Madejová, J., 2001, Weathering of smectite and illite-smectite under temperate climatic conditions: Clay Minerals, v. 36, p. 403–419, doi:10.1180/000985501750539490.

Svensen, H., Planke, S., Malthe-Sørenssen, A., Jamtveit, B., Myklebust, R., Eidem, T.R., and Rey, S.S., 2004, Release of methane from a volcanic basin as a mechanism for initial Eocene global warming: Nature, v. 429, p. 542–545, doi:10.1038/nature02566.

Thomas, L.E., 1965, Sedimentation and structural development of Big Horn basin: American Association of Petroleum Geologists Bulletin, v. 49, p. 1867–1877.

Van De Velde, J.H., Bowen, G.J., Passey, B.H., Bowen, B.B., 2013, Climatic and diagenetic signals in the stable isotope geochemistry of dolomitic paleosols spanning the Paleocene-Eocene boundary: Geochimica et Cosmochimica Acta, v. 109, p. 254–267, doi:10.1016/j.gca.2013.02.005.

Wang, C., Hong, H., Li, Z., Yin, K., Xie, J., Liang, G., Song, B., Song, E., and Zhang, K., 2013, The Eocene–Oligocene climate transition in the Tarim Basin, northwest China: Evidence from clay mineralogy: Applied Clay Science, v. 74, p. 10–19, doi:10.1016/j.clay.2012.09.003.

White, A.F., and Brantley, S.L., 2003, The effect of time on the weathering of silicate minerals: Why do weathering rates differ in the laboratory and field?: Chemical Geology, v. 202, p. 479–506, doi:10.1016/j.chemgeo.2003.03.001.

White, A.F., Blum, A.E., Schulz, M.S., Bullen, T.D., Harden, J.W., and Peterson, M.L., 1996, Chemical weathering of a soil chronosequence on granitic alluvium: I. Quantification of mineralogical and surface area changes and calculation of primary silicate reaction rates: Geochimica et Cosmochimica Acta, v. 60, p. 2533–2550, doi:10.1016/0016-7037(96)00106-8.

Wilson, M.J., 1999, The origin and formation of clay minerals in soils: Past, present and future perspectives: Clay Minerals, v. 34, p. 7–25, doi:10.1180/000985599545957.

Wing, S.L., Alroy, J., and Hickey, L.J., 1995, Plant and mammal diversity in the Paleocene to early Eocene of the Bighorn Basin: Palaeogeography, Palaeoclimatology, Palaeoecology, v. 115, p. 117–155, doi:10.1016/0031-0182(94)00109-L.

Wing, S.L., Harrington, G.J., Smith, F.A., Bloch, J.I., Boyer, D.M., and Freeman, K.H., 2005, Transient floral change and rapid global warming at the Paleocene-Eocene boundary: Science, v. 310, p. 993–996, doi:10.1126/science.1116913.

Worden, R.H., and Morad, S., 2003, Clay minerals in sandstones: Controls on formation, distribution and evolution, *in* Worden, R.H., and Morad, S., eds., Clay Mineral Cements in Sandstones: International Association of Sedimentologists Special Publication 34, p. 3–41, doi:10.1002/9781444304336.ch1.

Zachos, J.C., Röhl, U., Schellenberg, S.A., Sluijs, A., Hodell, D.A., Kelly, D.C., Thomas, E., Nicolo, M., Raffi, I., and Lourens, L.J., 2005, Rapid acidification of the ocean during the Paleocene-Eocene Thermal Maximum: Science, v. 308, p. 1611–1615, doi:10.1126/science.1109004.

Zacke, A., Voigt, S., Joachimski, M.M., Gale, A.S., Ward, D.J., and Tütken, T., 2009, Surface-water freshening and high-latitude river discharge in the Eocene North Sea: Journal of the Geological Society of London, v. 166, p. 969–980, doi:10.1144/0016-76492008-068.

Science Editor: Bradley S. Singer
Associate Editor: Benjamin J.C. Laabs

Manuscript Received 17 February 2016
Revised Manuscript Received 17 January 2017
Manuscript Accepted 7 March 2017

Printed in the USA